ADVANCED MATERIALS INTERFACES
www.advmatinterfaces.de

ALD-Coated Mesoporous Iridium-Titanium Mixed Oxides: Maximizing Iridium Utilization for an Outstanding OER Performance

Marvin Frisch, Muhammad Hamid Raza, Meng-Yang Ye, René Sachse, Benjamin Paul, René Gunder, Nicola Pinna, and Ralph Kraehnert**

Dedicated to Prof. Dr. Jürgen Caro on the occasion of his 70th birthday

With the increasing production of renewable energy and concomitant depletion of fossil resources, the demand for efficient water splitting electrocatalysts continues to grow. Iridium (Ir) and iridium oxides (IrO_x) are currently the most promising candidates for an efficient oxygen evolution reaction (OER) in acidic medium, which remains the bottleneck in water electrolysis. Yet, the extremely high costs for Ir hamper a widespread production of hydrogen (H_2) on an industrial scale. Herein, the authors report a concept for the synthesis of electrode coatings with template-controlled mesoporosity surface-modified with highly active Ir species. The improved utilization of noble metal species relies on the synthesis of soft-templated metal oxide supports and a subsequent shape-conformal deposition of Ir species via atomic layer deposition (ALD) at two different reaction temperatures. The study reveals that a minimum Ir content in the mesoporous titania-based support is mandatory to provide a sufficient electrical bulk conductivity. After ALD, a significantly enhanced OER activity results in dependency of the ALD cycle number and temperature. The most active developed electrocatalyst film achieves an outstanding mass-specific activity of 2622 mA mg_{Ir}^{-1} at 1.60 V_{RHE} in a rotating-disc electrode (RDE) setup at 25 °C using 0.5 M H_2SO_4 as a supporting electrolyte.

1. Introduction

The generation of H_2 by water electrolysis represents an attractive way to obtain clean energy and reduce the excessive consumption of fossil resources.[1–3] For a combination with intermittent power supplies from renewables, PEM water electrolysis using a polymer electrolyte membrane (PEM) is highly promising.[4,5] Disadvantageously, the oxygen evolution reaction (OER) occurring at the anode shows sluggish kinetics and, thus, hampers an efficient overall electrochemical water splitting.[5,6] Large-scale electrolysis demands for affordable and active electrocatalysts.[7] Ir-[8–10] and Ru-based[11,12] materials were identified to show the highest catalytic OER activities in acidic electrolytes. Due to their higher stabilities, Ir-based catalysts represent the state-of-the-art anode materials.[8,13,14] To improve the utilization of the active noble metal, different approaches have been made, e.g., alloying IrO_x with earth-abundant metal oxides (TiO_2,[15] Ta_2O_5,[16] SnO_2[17]), dispersing IrO_x in the form of nanocrystals on high-surface area support materials (Sb-doped SnO_2[18]), or the introduction of well-defined nanostructures by templating processes.[10,19] Yet, declined electrical conductivities were frequently reported after the addition of insulating transition metal oxides such as TiO_2[20] or Ta_2O_5.[21] Regarding the stability of the support materials, doping was shown to enhance corrosion resistance, yet, most support materials show low stabilities in acid.[22] The interested reader is referred to a comprehensive review by Maillard and co-workers.[23]

M. Frisch, M.-Y. Ye, B. Paul, R. Kraehnert
Department of Chemistry
Technische Universität Berlin
Strasse des 17. Juni 124, 10623 Berlin, Germany
E-mail: ralph.kraehnert@tu-berlin.de

The ORCID identification number(s) for the author(s) of this article can be found under https://doi.org/10.1002/admi.202102035.

DOI: 10.1002/admi.202102035

M. H. Raza, N. Pinna
Institut für Chemie and IRIS Adlershof
Humboldt-Universität zu Berlin
Brook-Taylor-Strasse 2, 12489 Berlin, Germany
E-mail: nicola.pinna@hu-berlin.de

R. Sachse
Federal Institute for Materials Research and Testing (BAM)
Unter den Eichen 44-46, 12203 Berlin, Germany

R. Gunder
Helmholtz-Zentrum Berlin für Materialien und Energie
Hahn-Meitner-Platz 1, 14109 Berlin, Germany

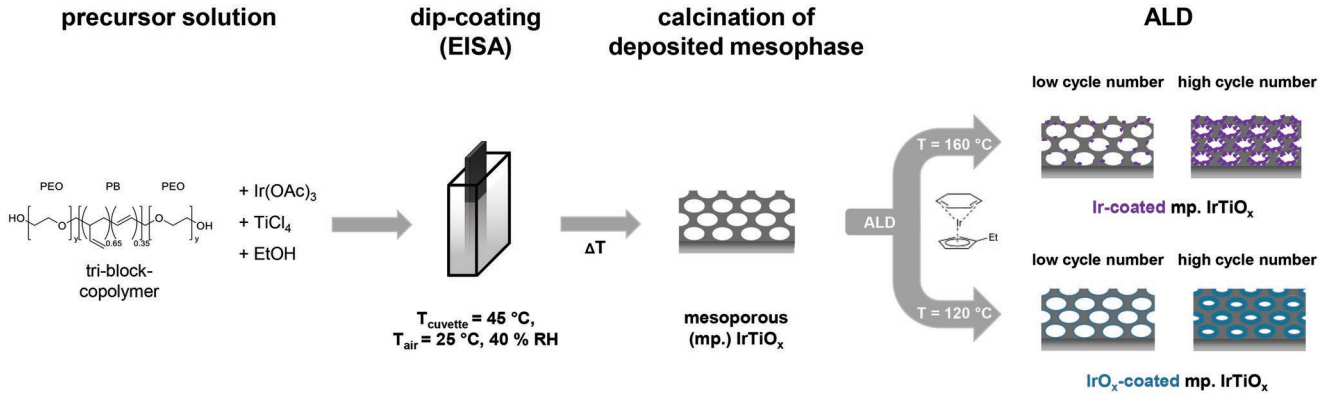

Scheme 1. Developed synthesis route for Ir- and IrO_x-coated mixed iridium titania catalysts in the form of mesoporous (mp.) films deposited on different planar substrates (Si, Ti, and glass). As a first step, a solution containing the metal precursors and a micelle-forming block-copolymer is deposited onto a substrate, dried and then calcined for 10 min at 375 °C in air to produce mesoporous iridium titania (mp. $Ir_{0.15}Ti_{0.85}O_2$, further denoted as mp. $IrTiO_x$). The obtained porous oxide support is subsequently exposed in alternating cycles to the ALD precursors (EtCp)Ir^{I}CHD and ozone (O_3) for the deposition of iridium (Ir) ($T_{Ir\text{-}ALD}$ = 160 °C) or iridium oxide (IrO_x) ($T_{IrOx\text{-}ALD}$ = 120 °C) over the entire external and internal surface of the oxides' pore systems. The obtained catalyst films show varying Ir loadings as a consequence of varying numbers of ALD cycles between 20 (low cycle number) and 60 (high cycle number).

For the design of superior electrocatalysts several key features are desirable, such as 1) a large number of active surface sites with 2) a good accessibility as well as 3) a sufficient electrical conductivity to promote charge transfer at the electrode interfaces, and 4) a sufficient stability of the catalyst against corrosion in OER regime.[24,25] As it is highly challenging to reach all of those requirements in a single catalyst material, we propose electrically conductive porous materials that fulfill requirements 2 and 3, surface-modified with thin, shape-conformal layers of a catalytically active and stable material to address requirements 1 and 4.

Mechanically stable and electrically conductive electrode coatings can be achieved by a method called evaporation-induced self-assembly (EISA).[26,27] The general synthesis concept relies on the application of a soft template, e.g., an amphiphilic block-copolymer, as a porogen to produce fully interconnected pore networks with adjustable pore diameters.[26–28] The EISA method is well-established and has been previously used to synthesize various mesoporous metal oxides such as SiO_2,[26] TiO_2,[29] IrO_x,[10] mixed metal oxides such as $IrTiO_x$[20,30] or Nb-doped TiO_x,[31] and composite materials such as Pd/TiO_2,[32] among others.

Atomic layer deposition (ALD) represents one of the most efficient ways to modify the entire surface of porous materials in a shape-conformal way, since ALD can ensure a highly conformal deposition of thin surface layers due to a self-limiting reaction mechanism.[33–37] The amount and surface layer thickness of the deposited species can be tuned by changing the number of ALD cycles.[34,38–40]

We illustrate the proposed concept for the example of mixed iridium titania films with template-controlled mesoporosity (mp. $IrTiO_x$) as a support material for IrO_x species deposited via ALD.

Summing up, we herein present the production of nanostructured acidic OER catalysts, in which the bulk consists of a sufficiently conductive iridium titanium mixed oxide support with the entire surface uniformly coated with an ultrathin layer of IrO_x deposited via conformal ALD. **Scheme 1** outlines the overall concept of the study. Based on our previous report,[30] we synthesized templated mesoporous $IrTiO_x$ films (15 mol%/30 wt% Ir content in the mixed oxide) on different flat substrates via dip-coating and EISA using titanium(IV)chloride ($TiCl_4$) and iridium(III)acetate ($Ir(OAc)_3$) as metal precursors and ethanol as a polar solvent. Subsequently, ALD was used to coat the entire internal and external surfaces of the conductive support with Ir species via alternating cycles of 1-ethylcyclopentadienyl-1,3-cyclohexadieneiridium(I) [(EtCp)Ir^{I}CHD] and ozone (O_3) pulses at two different temperatures (120 °C/160 °C). By tuning the temperature during ALD, the nature of the deposited Ir species was adjusted.[41,42]

In this work, we systematically investigate also fundamental aspects of the synthesis and electrochemical performance of IrO_x surface-modified electrode coatings. In particular, these are (a) the impact of the temperature at which ALD is performed (120 °C vs 160 °C), b) the role of the number of respective ALD cycles (0, 20, 40 and 60) and (c) the impact of ALD on the electrical properties of the mesoporous support.

2. Results and Discussion

2.1. Impact of ALD-Temperature and Cycle Number on the Morphology

As shown by representative top-view SEM images in **Figure 1**a, micelle-templated $IrTiO_x$ films were obtained via dip-coating and EISA. The corresponding fast Fourier transform (FFT, inset in Figure 1a) reveals an isotropic ring, thus indicating a locally-ordered mesoporous structure and a well-preserved template-controlled porosity in the films after calcination at 375 °C in air. These mp. $IrTiO_x$ films were then surface-modified using two different ALD processes at two different reaction temperatures. Pronounced differences become visible depending on the temperature during ALD. In brief, ALD at 160 °C leads to the formation of finely dispersed nanoparticles on the surface of the pore walls, whereas ALD at 120 °C affords dense surface Ir-rich layers covering the entire pore wall surface of the $IrTiO_x$ support. The influence of the ALD temperature and cycle number can be examined via SEM analysis. For low cycle numbers, i.e., 20 cycles, ALD at 160 °C leads to the presence of small Ir-rich nanoparticles

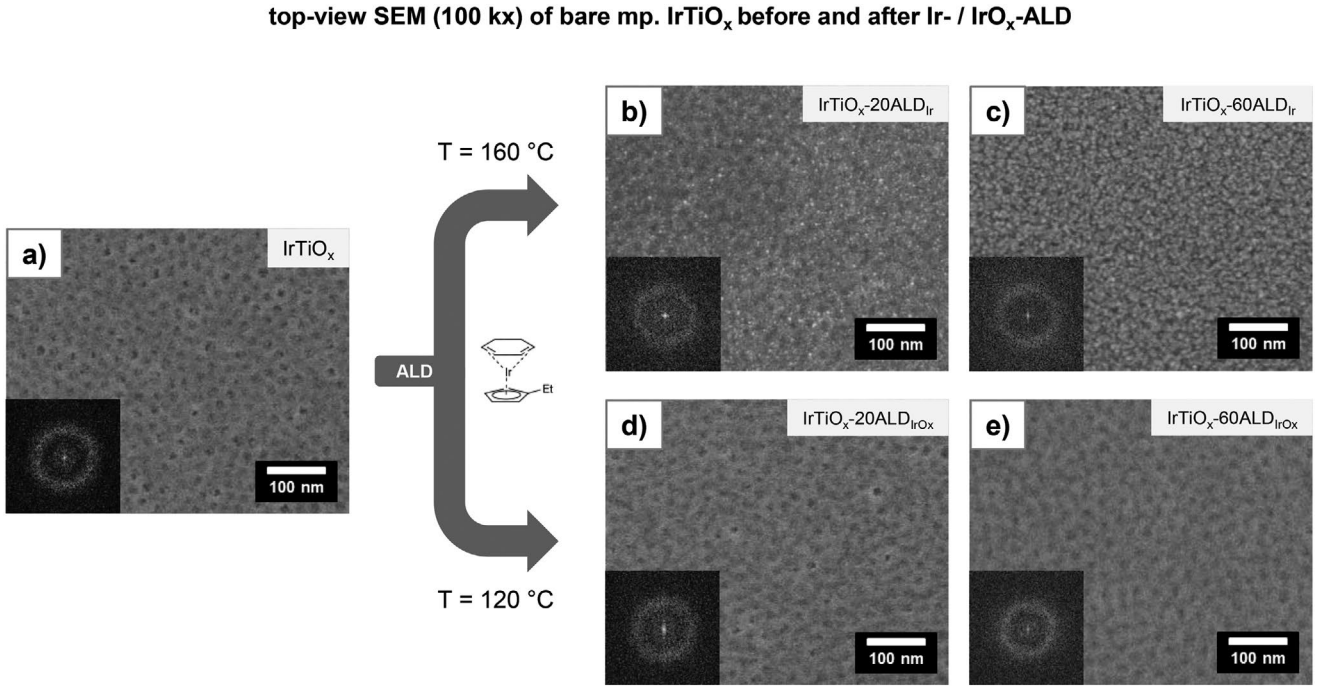

Figure 1. Representative top-view SEM images of mp. IrTiO$_x$ prior to a) and after surface-modification using ALD at b,c) 160 °C and at d,e) 120 °C. The corresponding ALD cycle number is denoted in the sample description. Insets on the bottom left corner of each image show the corresponding FFT. A diffuse ring in the FFT indicates the presence of a mesoporous structure, which is well-preserved after ALD. Distinct structural differences are visible depending on the temperature during the ALD process. High temperatures of 160 °C lead to the occurrence of nanoparticle-like deposits with bright contrast on the images, whereas lower temperatures of 120 °C lead to the formation of a homogeneous surface layer-type coating on the pore walls of the support.

of bright contrast, as evidenced by SEM images in Figure 1b. Still, the mesoporous structure remains essentially preserved, since the corresponding FFT reveals a diffuse ring (inset in Figure 1b).

With a higher cycle number of 60 ALD cycles at 160 °C, the structure of the pore walls has apparently changed and the mesopores appear partially blocked by the ALD deposits, according to SEM images depicted in Figure 1c. Nevertheless, the corresponding FFT inset provides evidence for a preserved mesoporous structure. A lower ALD temperature (120 °C) was applied, aiming at more layer-like structures rather than the formation of nanoparticulate surface species.[41,42] Apparently, SEM analysis nicely confirms the preservation of the template-introduced mesoporous structures after ALD at 120 °C (Figure 1d,e).

As reference support materials, bare TiO_2 films with template-controlled porosity were simultaneously modified via ALD at both 120 °C and 160 °C. Similar observations regarding the impact of temperature and cycle number of the ALD process on the resulting morphologies of the coatings were found (see Section I in the Supporting Information). Importantly, lower magnification SEM images suggest the formation of homogeneous films and the absence of larger, ill-defined aggregates for all investigated areas of samples (see Section II in the Supporting Information).

Our investigations clearly point out that the temperature during the ALD process is a key parameter to control the morphology of the deposited species. More specifically, ALD at 120 °C was found to be most suitable for the deposition of highly conformal, layer-like surface deposits. In the following section, the impact of the number of ALD cycles at 120 °C will be investigated in order to gain more insights into properties such as the layer thickness of the deposited surface layer.

2.2. ALD at 120 °C: Impact of Cycle Number on ALD-Layer Thickness and Pore Size

To further investigate the impact of ALD at 120 °C on the pore structure, the average pore diameters were analyzed and plotted as a function of the corresponding ALD cycle number (**Figure 2**b). IrTiO$_x$ films show spherical mesopores with an average pore diameter of 18 nm. After 20, 40, and 60 ALD cycles at 120 °C, decreasing average pore diameters of approximately 17, 16, and 15 nm were found, respectively. The observed linear correlation between the average pore diameter and the ALD cycle number results from an increase in ALD-layer thickness with an increasing number of ALD cycles, as further evidenced by results from spectroscopic ellipsometry (Figure 2a) with a calculated growth per cycle (GPC) of 0.7 ± 0.006 Å cycle^{-1} on flat silicon (Si) substrates. Vice versa, the average pore wall thickness rises for increasing cycle numbers, assuming a rigid porous framework obtained via calcination at elevated temperature.[43] Indeed, such a linear correlation is characteristic for ALD processes based on self-limiting surface reactions affording homogeneous surface coatings with high conformality and has been reported before.[41,44–46]

2.3. Impact of the Different ALD Processes at 120 °C and 160 °C on Phase and Crystallinity

To gain more insights into the structural properties such as the morphology, crystallinity, and phases prior to and after ALD, TEM, SAED, and GI-XRD analyses were performed. Calcination

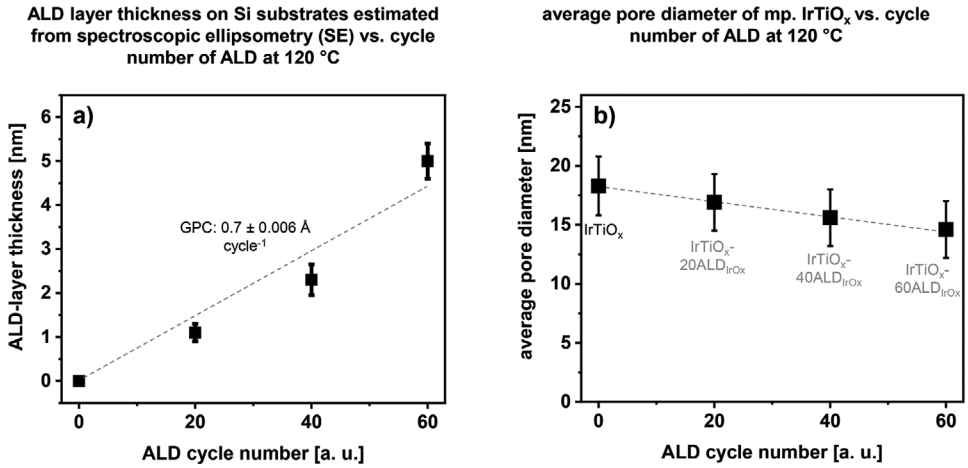

Figure 2. Plot showing the estimated layer thickness on Si substrates based on the results from spectroscopic ellipsometry (SE) versus ALD cycle number at a) 120 °C. Vertical bars indicate the respective standard deviations. A linear regression corresponding to a GPC of 0.7 Å cycle^{-1} was obtained after fitting of the data. In b), results from the pore size evaluations of mp. $IrTiO_x$ prior to and after ALD at 120 °C based on the SEM images shown in Figure 1 are given. Vertical bars indicate the respective error bars. The dashed gray lines were added to show a linear correlation between the average pore size and ALD cycle number.

of the mp. $IrTiO_x$ support for 10 min at 375 °C leads to a low crystalline oxide (**Figure 3**a,IV, SAED pattern) with template-controlled mesoporous structure, as indicated by the TEM images shown in Figure 3aI,II. EDX analysis and elemental mappings (Section IV in the Supporting Information) reveal a homogeneous distribution of Ir throughout the support.

Again, the temperature during ALD is found to show a distinct impact on the morphology, phase, and crystallinity of the deposited surface layers. In this context, ALD at 160 °C affords small, nanoparticulate Ir surface species, according to the HRTEM image depicted in Figure 3b-III.

The lattice fringes in the inset of the HRTEM image, the power spectrum (PS) of the selected region in Figure 3b-III as well as the SAED pattern in Figure 3b-IV suggest the presence of lattice fringes corresponding to metallic Ir^0 crystallites introduced via ALD. Similarly, XRD analysis in gracing-incidence geometry provides further evidence for the deposition of Ir^0 species via ALD at 160 °C, since additional reflections appear that match well with a nanocrystalline, metallic Ir phase (see Section VII in the Supporting Information). This observation is corroborated by SEM (see Figure 1a,b, right) and XPS analyses. Surface-sensitive XPS analysis reveals a significantly increased fraction of metallic Ir^0 species after ALD at 160 °C (see Section V in the Supporting Information for more details). In this context, the relative fraction of Ir^0 species (respective to the total amount of surface Ir) rises from ≈8 at% in mp. $IrTiO_x$ to ≈75 at% after 60 cycles ALD at 160 °C. For the mp. TiO_2 support films, similar results were obtained from TEM (Section III in the Supporting Information) and XPS (Section V in the Supporting Information) analyses, which underlines the predominance of mainly metallic Ir^0 deposits after ALD at 160 °C independent of the support material.

Contrarily, after ALD at 120 °C, weak signals corresponding to the onset of crystallization of rutile-type IrO_2 can be identified in the SAED pattern of ALD-coated $IrTiO_x$ (Figure 3c-IV). In addition, the low crystallinity of the ALD deposits is confirmed by GI-XRD analysis which did not reveal the appearance of additional reflections (Section VII in the Supporting Information). According to XPS results, prior to ALD, the predominant surface species can be assigned to Ir^{3+} (see Ir 4f spectrum of mp. $IrTiO_x$ in Figure S5a, Supporting Information, top) with a minor contribution of metallic Ir^0.[47,48] The latter completely vanishes after only 20 cycles ALD due to the observation that the Ir 4f spectrum of $IrTiO_x$-$20ALD_{IrOx}$ is dominated by Ir^{3+} species at its surface (see Figure S6b, Supporting Information, top). For 60 cycles of ALD at 120 °C, the ratio of surface Ir/Ti increases, as expected for higher loadings of IrO_x for higher cycle numbers (Table S2, Supporting Information). Hence, for $IrTiO_x$ support films modified via ALD at 120 °C, a structural model based on a mesoporous mixed iridium titanium oxide with low Ir content inside the bulk and high Ir concentration at the pore wall surface due to a homogeneous coating with predominantly oxidic Ir^{3+} species can be deduced. For TiO_2 supports modified via ALD at 120 °C, a similar structure with a noble-metal free bulk can be claimed. This nanostructure enables a maximized exposure of active Ir sites for electrochemical applications with the aim of improving the mass-specific OER activity. Importantly, the mesoporous structure remains well-preserved even after high ALD cycle numbers, thus avoiding mass-transfer limitations during catalysis.

2.4. Impact of ALD Temperature and Cycle Number on the Electrical Properties and OER Activity

Impedance spectroscopy is a powerful tool to assess the electrical conductivities of thin films deposited on insulating substrates.[31,49] In accordance with our previous results[20,30] for as-prepared mesoporous films prior to catalytic testing, the addition of 15 mol% Ir to TiO_x leads to well-conductive materials (≈10^{-2} S cm^{-1} for mp. $IrTiO_x$), which enables efficient charge transfer kinetics at the electrode during OER catalysis.[20] According to the results given in **Figure 4**a and **Table 1**, both ALD processes lead to a rise in conductivity for increasing ALD cycle numbers. The impact of the number of ALD cycles on the electrical conductivity is significantly more pronounced than the influence of the ALD temperature in the case of the mp. TiO_2 supported films (see Section VIII in the

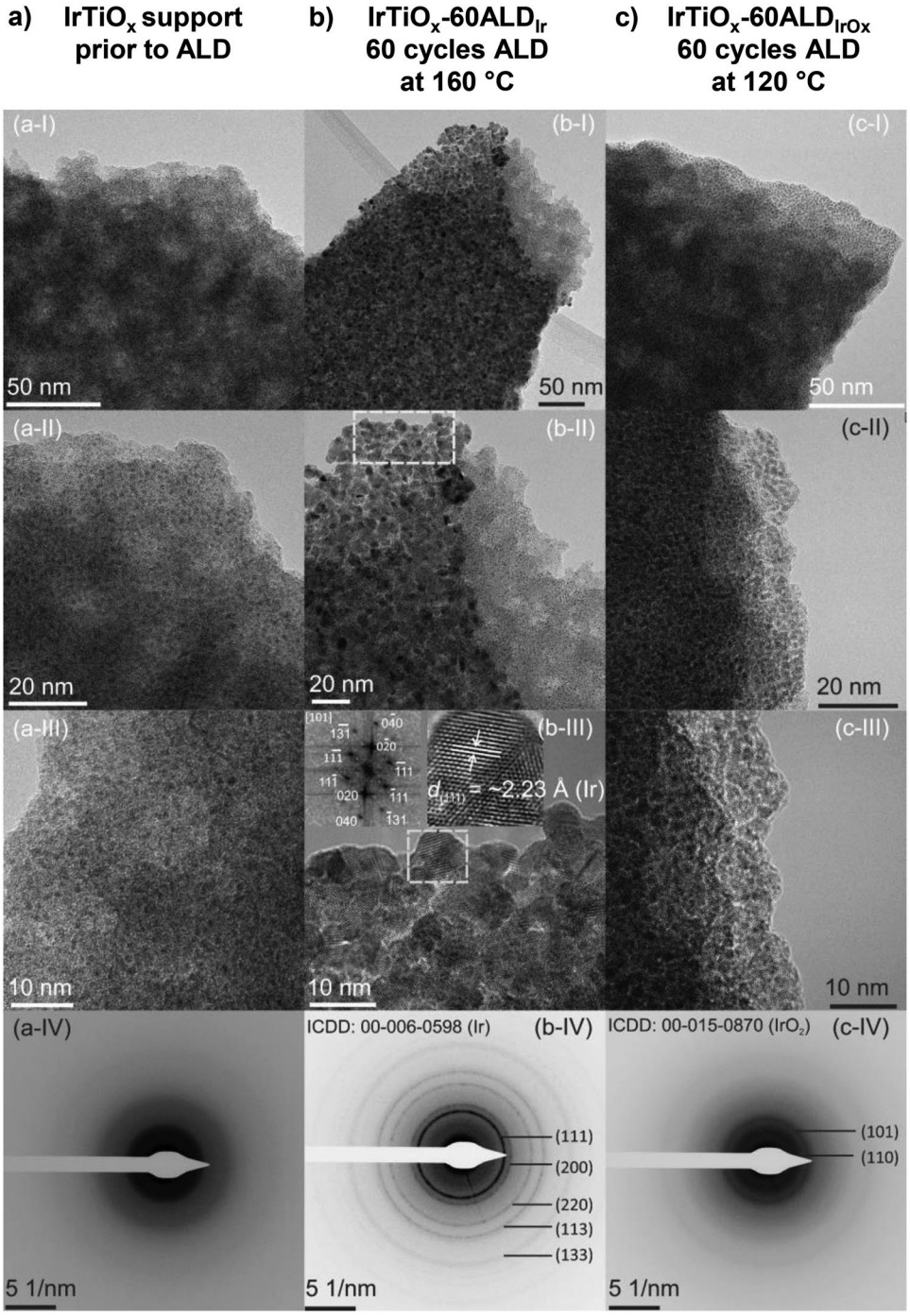

Figure 3. BF-HRTEM images (I–III) and SAED patterns (IV) for a) the mp. IrTiO$_x$ support, b) after 60 cycles of ALD at 160 °C (IrTiO$_x$-60ALD$_{Ir}$) and c) after 60 cycles ALD at 120 °C (IrTiO$_x$-60ALD$_{IrOx}$). In b-III) the upper left inset shows the obtained power spectrum (PS) of the area in the HRTEM image highlighted by the white frame. The patterns in IV are assigned according to the reference ICDD card numbers 00-006-0598 for Ir^0 (cubic) and 00-015-0870 for IrO_2 (tetragonal), respectively.

Supporting Information for further discussion). Notably, after 60 cycles of ALD at both 120 °C and 160 °C, well-conductive coatings were obtained showing similar sheet conductivities between ≈10^1 to ≈10^3 S cm^{-1}, independent of the support. These findings are in good agreement with the high conductivities of both metallic and oxidic Ir phases. Due to the fact that the evaluated sheet conductivity values for high cycle numbers of Ir- and IrO$_x$–ALD lie within a similar range (taking minor measurement errors into account), both types of surface modifications clearly improve the electrical properties of the TiO_2- and IrTiO$_x$-based materials by several orders of magnitude.

To assess the impact of both temperature and number of ALD cycles on the catalytic OER activity, RDE measurements were conducted in N_2-purged 0.5 M sulfuric acid at

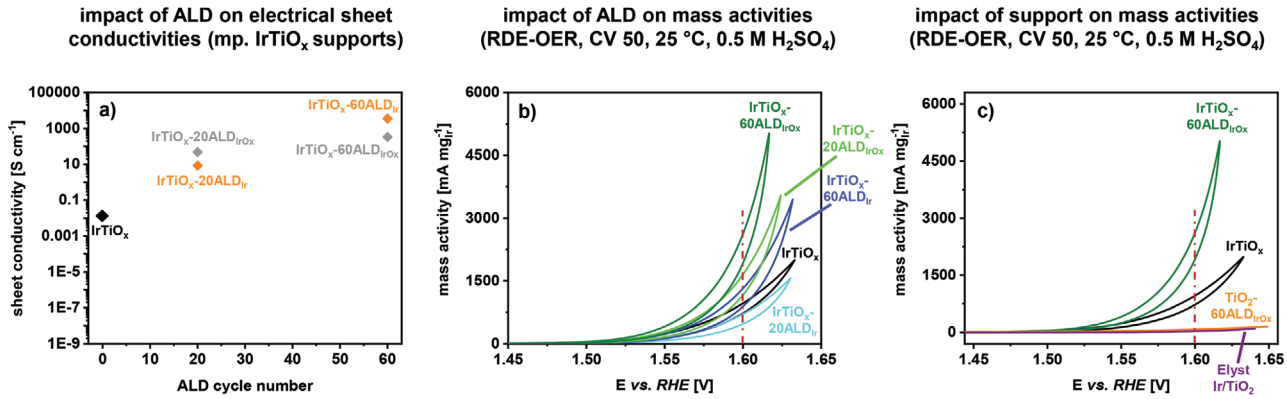

Figure 4. a) Electrical sheet conductivities assessed via impedance spectroscopy of mp. $IrTiO_x$ (black rhomb) as well as $IrTiO_x$ supports modified via ALD at 160 °C (orange) and at 120 °C (gray). All investigated films were deposited on insulating glass substrates. b) Ir mass-normalized activities of the bare mp. $IrTiO_x$ support (black) in comparison with the ALD-modified $IrTiO_x$ supports. Light and dark green curves represent supports modified via IrO_x–ALD at 120 °C with 20 and 60 ALD cycles, respectively. Light and dark blue curves represent supports modified via Ir–ALD at 160 °C with 20 and 60 cycles, respectively. c) Mass activities of the most active catalyst film $IrTiO_x$–$60ALD_{IrOx}$ (dark green) and the bare mp. $IrTiO_x$ support (black) in comparison with the commercial reference Elyst Ir75 (purple) and TiO_2-$60ALD_{IrOx}$ produced via 60 cycles ALD at 120 °C on a mp. TiO_2 support (orange). All electrochemical testings were conducted in an RDE setup and N_2-purged 0.5 M H_2SO_4 at 25 °C. The 50th CV is plotted for each catalyst film deposited on polished Ti substrates. It has to be noted that Nafion binder was added for the measurement of the reference catalyst powder. The dashed vertical red lines in (b–c) serve as a guideline to the eye.

room temperature for all films listed in Table 1. From the electrochemical testings, values for the Tafel slopes, Ir mass-normalized activities and the relative numbers of accessible active surface Ir sites (determination based on voltammetric charge using a previously established method described elsewhere[20,50]) of the catalysts were derived. Table 1 provides an overview of the electrical properties and the electrochemical performance data prior to and after ALD. Figure 4b shows the Ir-mass based activity plots of the 50th CVs for $IrTiO_x$ and ALD-modified $IrTiO_x$ films. Both, ALD temperature and cycle number affect the calculated Ir mass-normalized catalytic activities. With respect to the bare mp. $IrTiO_x$ support, improved mass activities can be achieved after the optimization of the ALD temperature and cycle number. In this context, ALD at 120 °C affords more active catalyst films than those produced via ALD at 160 °C.

At a potential of 1.60 V_{RHE}, mp. $IrTiO_x$ achieves a mass-normalized OER activity of 962 mA mg_{Ir}^{-1}, which can be explained by the presence of highly active Ir domains in a TiO_2 matrix produced via calcination at benign temperatures.[30] After 20 cycles of Ir-ALD at 160 °C, a slight drop in mass activity to 706 mA mg_{Ir}^{-1} can be observed. Importantly, deposition via ALD produces different types of Ir species compared to thermal treatments. In this context, our previous works[19,20,30,51] revealed a strong correlation between activity and calcination temperature for mesoporous Ir-based OER catalyst model

Table 1. Overview over the electrical properties and electrocatalytic RDE-OER performance in 0.5 M H_2SO_4 (25 °C) of mp. $IrTiO_x$ prior to and after ALD at 120 °C and 160 °C. As references, catalysts supported using low conductive mp. TiO_2 and the commercial Ir/TiO_2 powder (Elyst, Umicore) are given.

Catalyst	ALD cycle number	ALD temperature [°C]	Ir loading[a)] [µg cm^{-2} geom. area]	Conductivity[b)] [S cm^{-1}]	Charge $q_{(a+c)/2}$[c)] [mC]	η (1 mA cm^{-2}, CV 50) [mV]	η (10 mA cm^{-2}, CV 50) [mV]	Mass activity (1.60 V, CV 50) [A g_{Ir}^{-1}]	Tafel slope[d)] (CV 50) [mV dec^{-1}]
$IrTiO_x$	0	–	3.9	≈10^{-2}	0.30	323	414	962	69
$IrTiO_x$–$20ALD_{Ir}$	20	160	6.3	≈10^{1}	0.71	323	402	706	64
$IrTiO_x$–$60ALD_{Ir}$	60	160	9.2	≈10^{3}	0.78	302	364	1318	57
$IrTiO_x$–$20ALD_{IrOx}$	20	120	5.5	≈10^{2}	0.43	308	373	1651	59
$IrTiO_x$-$60ALD_{IrOx}$	60	120	7.0	≈10^{3}	0.93	296	353	2622	55
TiO_2-$60ALD_{IrOx}$	60	120	5.9	≈10^{2}	0.43	424	*	79	139
Ref. Elyst Ir/TiO_2 (powder)	0	–	≈80	–	0.42	344	421	30	65

[a)]Average geometric Ir loading determined via quantitative SEM-EDX measurements on Ti substrates, except for the reference catalyst powder Elyst (nominal loading). For the unmodified supports, ICP-OES measurements were performed to confirm the EDX-derived geometric Ir loadings (see Experimental Section); [b)]Electrical conductivity investigated via impedance spectroscopy in the dark; [c)]Voltammetric charge assessed via base voltammetry in a lower potential range between 0.4 to 1.4 V_{RHE} (see Section IX in the Supporting Information) as an estimate for the electrochemically active surface Ir species; [d)]Tafel plots are given in Figure S11 in the Supporting Information. An asterisk (*) indicates that the respective current density was not reached within the investigated potential range.

systems. Our previous findings indicate a deposition of predominantly metallic Ir^0 species via ALD at 160 °C. Due to the fact that the voltammetric charge (see Table 1) is more than two-fold higher for $IrTiO_x$-$20ALD_{Ir}$ than that of the $IrTiO_x$ support, a lower intrinsic activity of the ALD-deposited Ir^0 species can be claimed. After 60 ALD cycles at 160 °C, a higher mass activity of 1318 mA mg_{Ir}^{-1} is achieved, which can be explained by the larger number of nanoparticulate Ir^0 deposits providing more active surface Ir sites overall. As suggested from investigations of the electrical conductivities, neighboring crystallites are in close contact to each other and provide additional electron paths at the surface and, thereby, promote OER activity.[44,45,52]

Yet, ALD at 120 °C affords significantly more active catalysts. $IrTiO_x$-$60ALD_{IrOx}$ achieves the highest OER activity of 2622 mA mg_{Ir}^{-1} at 1.60 V_{RHE}, which is more than 2.7-fold higher than that of the unmodified mp. $IrTiO_x$ support (see Figure 4b,c). The outstanding Ir mass-specific activities of the ALD-modified $IrTiO_x$ catalysts can be deduced from the ultra-low loading and high accessibility of the well-dispersed IrO_x active centers at the surface of the porous support. The optimization of the ALD process is primordial to achieve a highly conformal and homogeneous deposition of oxidic Ir^{x+} species of low crystallinity. Notably, XPS analyses of the oxidation states of the surface Ir species for the spent catalysts modified via Ir-ALD at 160 °C indicate a significant fraction of unoxidized Ir^0 (see Section V in the Supporting Information), highlighting the necessity to adjust the ALD parameters in order to improve the intrinsic activities of the active sites. Moreover, all herein developed catalyst coatings are binder-free films which have been shown to be more active than Nafion-containing catalyst films.[53]

Amongst state-of-the-art Ir–Ti-based electrocatalysts, all herein developed ALD-modified $IrTiO_x$ films achieve a significantly improved OER performance with outstanding Ir mass-specific activities in acidic electrolyte (**Table 2**). Remarkably, despite the ultralow Ir loadings, an exceptionally high mass activity of 178 mA mg_{Ir}^{-1} at 1.53 V_{RHE} can be achieved for the most active binder-free coating, i.e., $IrTiO_x$-$60ALD_{IrOx}$, that is even higher than that of the "stellar" $IrO_x/SrIrO_3$ catalyst.[9,61,62] With respect to mp. IrO_x films calcined for 10 min at 375 °C in air,[19] a ≈1.8-fold higher mass activity reflects the superior noble metal utilization as a result from our proposed concept relying on a combination of EISA and ALD processes for the synthesis of a conductive support and post-modification of its surface with highly active species, respectively.

Importantly, our results from chronopotentiometric stability tests (see Section XIII in the Supporting Information) in acidic electrolyte indicate a remarkably improved durability after IrO_x–ALD. Compared to the unmodified $IrTiO_x$ support, $IrTiO_x$–$60ALD_{IrOx}$ shows a higher stability in acid and better protection from undesired dissolution into the surrounding electrolyte at moderate potentials and static operation as a result of the highly conformal ALD. Post-OER analysis of the

Table 2. Comparison of the most active catalysts in this work with RDE-OER activities of literature-reported Ir-based electrocatalysts (acidic electrolyte, 25 °C).

Catalyst	Ir content	Electrolyte	Electrode	Binder	η [V] (1 mA cm^{-2})	η [V] (10 mA cm^{-2})	Mass activity[a] [A g_{Ir}^{-1}]	Refs.
$IrTiO_x$–$60ALD_{IrOx}$	25 mol%	0.5 M H_2SO_4	Ti chip	Binder free	0.30	0.35	2622	This work
mp. $IrTiO_x$	15 mol% (30 wt%)	0.5 M H_2SO_4	Ti chip	Binder free	0.32	0.41	962	This work
mp. IrO_x (375 °C air)	100 mol%	0.5 M H_2SO_4	Ti chip	Binder free	0.25	0.29	1410	This work
Thermally decomposed Ir/TiO_x	30 mol%	1.0 M $HClO_4$	Ti	Binder free	n. a.	n. a.	39	[54]
ALD–IrO_2/NTO	8 wt%	0.5 M H_2SO_4	Ti foil	Binder free	0.25	n. a.	654 (at 1.69 V)	[55]
ALD-Ir/TiO_2-NTs[b]	n. a.	0.1 M H_2SO_4	TiO_2–NTs	Binder free	n. a.	0.24	200 (at 1.57 V)	[45]
IrO_2@TiO_2	26 mol%	0.1 M $HClO_4$	GC[c]	Nafion binder	n. a.	n. a.	364	[56]
IrO_2/Nb-doped TiO_2	26 wt%	0.5 M H_2SO_4	GC	Nafion binder	0.27	n. a.	≈ 550	[57]
IrO_2–TiO_2-245	40 mol%	0.1 M $HClO_4$	GC	Nafion binder	n. a.	n. a.	≈70 (at 1.53 V)	[58]
IrO_2/ATO	25 wt%	0.5 M H_2SO_4	GC	Nafion binder	0.22	n. a.	≈1100	[59]
$IrNiO_x$/Meso-ATO	19 wt%	0.05 M H_2SO_4	GC	Nafion binder	0.28	n. a.	≈90 (at 1.51 V)	[60]
6H-$SrIrO_3$	59 mol%	0.5 M H_2SO_4	GC	Nafion binder	n. a.	0.25	≈75 (at 1.53 V)	[61]
β-H_xIrO_3	79 mol%	1.0 M H_2SO_4	GC	Nafion binder	n. a.	0.35	≈150 (at 1.58 V)	[62]
Ir-nano 99.8-P	100 mol%	0.5 M H_2SO_4	GC	Nafion binder	n. a.	n. a.	≈580 (at 1.56 V)	[63]

[a]Mass activities calculated based on the loading amounts of active species in the catalysts at a potential of 1.60 V_{RHE} (unless otherwise stated). For the herein developed catalysts, geometric Ir loadings were analyzed via quantitative SEM-EDX measurements. Moreover, the Ir-normalized mass activities were derived from the current densities of the 50th CV in an RDE setup at 1.60 V_{RHE}; [b]NTs, nanotubes; [c]GC, glassy carbon.

spent catalysts via SEM-EDX revealed a significant loss (≈90%) of Ir species for bare mp. $IrTiO_x$, whereas the geometric Ir loading was essentially unaltered for $IrTiO_x$–$60ALD_{IrOx}$. It has to be noted that further investigations will be necessary in order to assess the electrode durability at fluctuating potentials over a broad current range and dynamic operation (see Section XIII in the Supporting Information for discussion).

2.5. Impact of Support Material on OER Activity

According to the results from the electrochemical studies, not only the temperature and cycle number of the ALD process emerge as decisive parameters for high catalytic activities but also the presence of a minimum of Ir in the bulk phase of the mesoporous support is required to promote fast charge transfer kinetics at the electrode. ALD-modified TiO_2-supported catalysts show significantly lower OER activities than their $IrTiO_x$-supported counterparts, despite the formation of conductive surface electron pathways, indicated by steeply rising sheet conductivities after 60 cycles ALD (cf. Section VIII in the Supporting Information).

Evidently, a high electrical conductivity in the bulk of the catalyst is essential to promote charge carrier kinetics and, beyond that, balance the overall charge of the material during OER by reversible proton insertion.[62] Our results suggest that the incorporation of 15 mol% of Ir into the titania-based support improves both the bulk electrical conductivity and the proton diffusivity and, thus, boosts catalytic activity after surface-modification with IrO_x via ALD at 120 °C. Analyses of the Tafel slopes summarized in Table 1 further corroborate the impact of the support on the catalytic activities. For TiO_2-supported catalysts, large values of more than 100 mV dec^{-1} were found (see also Section XI in the Supporting Information). Contrarily, $IrTiO_x$-supported catalysts show smaller values between 69 and 55 mV dec^{-1} with decreasing slopes for higher ALD cycle numbers, indicating faster reaction kinetics. Accordingly, a high electrical conductivity of the support material for ALD-deposited active sites plays an essential role in the design of active electrocatalysts with strong interactions between the surface metal (oxide) species and the support.

3. Conclusion

A sophisticated concept for the design of highly efficient OER catalyst coatings based on electrically conductive porous supports surface-modified with thin, shape-conformal layers of a catalytically active species was successfully developed. Therein, an optimized ALD process was used to ensure the deposition of layer-like oxidic Ir^{x+} surface species on a well-conductive mixed iridium-titanium oxide support with template-controlled mesoporosity (mp. $IrTiO_x$). A sufficient electrical bulk conductivity of the mesoporous support is a key prerequisite to reach high OER activities. The most active system, $IrTiO_x$–$60ALD_{IrOx}$, achieves an outstanding mass-specific OER activity of 2622 A g_{Ir}^{-1} at 1.60 V_{RHE} in a typical RDE setup at 25 °C and 0.5 M H_2SO_4 as a supporting electrolyte, which can be explained by the predominance of well-accessible, active oxidic Ir^{x+} sites. Highly conformal ALD at 120 °C paves the way toward a maximized utilization of these homogeneously distributed Ir species, culminating in a 2.7-fold higher Ir mass-specific activity than that of the unmodified mp. $IrTiO_x$ support.

As an outlook, our proposed concept can be principally transferred to other support materials and surface-exposed active species introduced via conformal ALD. As such, we expect the concept as highly promising for the future development of highly efficient (electro-)catalysts with an improved utilization of active sites.

4. Experimental Section

Material Synthesis: Substrate Pretreatments: For the deposition of the soft-templated mesoporous support films, different substrates were used. Single-side polished silicon (Si) wafers were obtained from University Wafers with (100) orientation and cleaned with EtOH after a thermal treatment for 2 h at 600 °C in air prior to the deposition of the support films. For the electrical sheet conductivity measurements, quartz glass (SiO_2) substrates bought from Science Services GmbH were used and etched prior to film deposition using a mixture of KOH and ^{i}PrOH in an ultrasonic bath. Electrochemical measurements were conducted on films deposited on electrically conductive titanium (Ti) substrates, polished with a colloidal silica suspension (amorphous, 0.02 µm, Buehler, MasterMet 2) and subsequently cleaned using a mixture of EtOH and ^{i}PrOH (1:1).

Material Synthesis: Synthesis of Soft-Templated Mesoporous TiO_2 Films: For the synthesis of mesoporous TiO_2 films, titanium(IV)chloride ($TiCl_4$, > 99.9%) was purchased from Sigma–Aldrich. Ethanol p. a. (EtOH, ≥99.8%) was purchased from VWR Chemicals. As structure-directing agent, a triblock copolymer PEO-PB-PEO, comprised of 20 400 g mol^{-1} polyethylene oxide (PEO) and 10 000 g mol^{-1} polybutadiene (PB), was purchased from Polymer Service Merseburg GmbH.[10] All chemicals were used as received without any further purification.

In a typical synthesis, the PEO-PB-PEO polymer template (75 mg) was dissolved in EtOH (2.00 mL) under stirring at 40 °C in air (I). $TiCl_4$ (232 µL) was dissolved in a closed vial in EtOH (2.00 mL) in an Ar-filled glovebox and added to solution (I). The obtained clear solution (II) was stirred for a further 30 min at 40 °C. Dip-coating was performed in air at 25 °C ambient temperature, 40% relative humidity (RH) and 300 mm min^{-1} withdrawal rate. The cuvette (PTFE) containing the clear precursor solution (II) was constantly heated to $T_{cuvette}$ = 45 °C. After drying for at least 10 min in a controlled atmosphere inside the dip-coating setup, crack-free colored films were obtained on different substrates. After drying for at least 1 h at 80 °C in air, all samples were calcined for 20 min at 475 °C in air with a heating ramp of 2 K min^{-1} in a muffle furnace.

Material Synthesis: Synthesis of Soft-Templated Mesoporous $IrTiO_x$ Films: The PEO-PB-PEO polymer template (60 mg) was dissolved in EtOH (1.50 mL) under stirring at 40 °C in air (III). $TiCl_4$ (114 µL) was dissolved in a closed vial in EtOH (1.50 mL) in an Ar-filled glovebox and added to solution (**III**). The obtained clear solution (**IV**) was stirred for a further 20 min at 40 °C. Then, iridium acetate (68 mg, $Ir(OAc)_3$, Heraeus, 48.76% Ir content) was added under stirring to (IV). A dark green, clear solution (V) was obtained after stirring for a further 30 min at 40 °C. Dip-coating was performed in air at 25 °C ambient temperature, 40% RH and 250 mm min^{-1} withdrawal rate. The cuvette was constantly heated to $T_{cuvette}$ = 45 °C. After drying for at least 10 min in a controlled atmosphere inside the dip-coating setup, crack-free colored films were obtained on different substrates. Calcination was conducted for 10 min at 375 °C in air in a preheated muffle furnace.

Material Synthesis: ALD on Different Mesoporous Supports: 1-Ethylcyclopentadienyl-1,3-cyclohexadieneiridium(I) [(EtCp)Ir^{1}CHD, 99%] was purchased from abcr GmbH. Ozone (O_3) was produced from oxygen (O_2, 99%) in an AC-2025 ozone generator-2000, Teledyne API. Nitrogen (N_2), argon (Ar), and O_2 were supplied by Air Liquide (99.9%).

Ir/IrO_x species were deposited on mesoporous films, i.e., mp. TiO_2, mp. $IrTiO_x$ on flat Ti, Si or quartz substrates. Additionally, pre-cleaned single-side polished Si-wafers (Siegert Wafer B014002) with a native SiO_2 layer (≈ 1.2–1.8 nm) were also added into the ALD chamber for calibration of the Ir/IrO_x layer thicknesses via spectroscopic ellipsometry (SE). ALD was performed in a thermal ALD system by ARRADIANCE (GEMStar-XT).

[(EtCp)Ir^{I}CHD] (at 90 °C) and O_3 (as-generated at rt.) were used as metal precursor and oxygen source, respectively. The Ir precursor and the O_2 source were supplied to the reaction chamber using two separate manifolds that were maintained at 110 °C and 100 °C, respectively. N_2 was used as a carrier gas (at 50 sccm) for the precursors into the reaction chamber, and also as a purging gas (at 100 sccm) for excess of reactants and by-products. The ALD system was evacuated (≈7 mTorr) and the temperature of the ALD reaction chamber was stabilized at 160 °C or 120 °C before starting the deposition. Prior to ALD, all samples were in situ treated with O_3 (10 cycles of 0.2 s O_3 pulse/30 s exposure/15 s purge, total exposure time of 300 s) to remove any residual organic surface impurities and to functionalize the surface. The pulse/exposure/purge time for one ALD cycle was set to 0.8 s/40 s/20 s and 0.25 s/45 s /30 s for Ir precursor and O_3, respectively. For the Ir precursor, the pulse/exposure/purge time was repeated two times within one ALD cycle. The loading of the deposited Ir/IrO_x species on the mesoporous films was controlled by varying the number of ALD cycles from 20 to 60.

Physicochemical Characterization: SEM and EDX: SEM images were recorded at 10 kV on a JEOL JSM-7401F instrument. The acquired images were then evaluated using ImageJ freeware (v. 1.48; www.imagej.nih.gov/ij/), which was also applied for the generation of the corresponding FFT images. For the estimation of the Ir mass loadings per cm^2 geometric area, SEM-EDX measurements were conducted using a Quantax 400 (Bruker) energy-dispersive X-ray spectrometer coupled with an electrometer model 6517B (Keithley) to determine the probe currents. For the latter, a Faraday cup was used to catch back-scattered, secondary and Auger electrons. An average value for the probe current was calculated based on the acquired values prior to and after the acquisition of an EDX spectrum of a material. For each sample, at least three different areas were analyzed via EDX analysis at a magnification of 1 kx. The measurement duration was set to at least 120 s. For the evaluation of the acquired EDX spectra, the software Esprit (Bruker) was used. A charge-and time-normalized signal intensity was obtained by dividing the average value of the Ir-Mα_1 and -M$_\beta$ lines by the average probe current and measurement duration. Quantitative Ir mass loadings were finally calculated by using a previously determined calibration factor evaluated from reference measurements of samples with Ir loadings validated via StrataGem analysis.[64,65] K-values were estimated from measurements of Ir metal (99.8%). Measurement errors were found negligible with only between 1% to 2% relative error.

ICP-OES: As an alternative method to analyze the geometric Ir loadings of the catalyst support films prior to ALD, ICP-OES measurements of the uncalcined mesophases deposited on flat Ti substrates were performed. Measurements were conducted on a Varian ICP-OES 715 ES (radial configuration, CCD detector). For calibration, aqueous solutions with different Ir concentrations (Carl Roth) were prepared. For the calculation of the geometric Ir loading, the geometric area of each film was calculated using ImageJ software prior to dissolution of the sample. For the dissolution of the samples via acid digestion, a solution of HCl (3.0 mL, Carl Roth, 37%), HNO_3 (1.0 mL, Carl Roth, 69%), H_2SO_4 (1.0 mL, Carl Roth, 96%) and $NaClO_3$ (20.0 mg, Alfa Aesar, 99.0%) was prepared. After 2 h at 30 °C in an ultrasonic bath, a clear solution was obtained and analyzed via ICP-OES to estimate the Ir content. For the TiO_2 support, essentially no Ir was found (0.0 μg_{Ir} cm^{-2}) and for $IrTiO_x$ a loading of 3.8 ± 0.3 μg_{Ir} cm^{-2} was obtained, which is in good agreement with EDX-derived geometric Ir loadings.

PTEM, EDX, and SAED: TEM images were acquired on a FEI Talos transmission electron microscope with 200 kV acceleration voltage on scraped-off film fragments which were deposited on carbon-coated copper grids. A FEI Talos EDX detector was used for the analysis of the elemental distributions via elemental mappings. The TEM data and EDX mappings were analyzed using FEI Velox software (v. 2.6).

XPS: X-ray photoelectron spectra (XPS) were obtained on a Thermo Fisher Scientific ESCALAB 250Xi with 400 µm spot size, K_α-X-rays. The peak position of adventitious carbon species at the surface (at a BE of 284.80 eV) was applied for correction of the binding energies of the obtained spectra. Data fitting and quantification to calculate the elemental composition were done using the software Avantage.

GI-XRD: XRD measurements were conducted using a Bruker D8 Advance instrument (Cu-K-α) in grazing-incidence geometry applying a Goebel mirror.

Electrical Sheet Conductivity: The electrical sheet conductivities were analyzed via impedance spectroscopy in a home-built setup in the dark. All measurements were carried out applying a 8 × 8 gold pin array as a probe head showing an altering polarity sequence. A SP-200 potentiostat (Biologic) was used (range from 100 mHz to 1 kHz). The obtained spectra (Nyquist impedance) were fitted using EIS Zfit software (EC-Lab version 11.33, Biologic). All given values were normalized to the average film thickness, estimated from cross-sectional SEM images of films deposited on Si substrates. For the impedance spectroscopy measurements, all films were deposited on planar, insulating quartz glass substrates.

Electrochemical Testing Procedure: OER Performance: All catalysts were tested in acidic OER via cyclic voltammetry (CV) performed using a rotating disc electrode setup (RDE). A reversible hydrogen electrode (Gaskatel, HydroFlex) was applied as a reference electrode and a Pt-gauze (Chempur, 1024 mesh cm^{-2}, wire diameter 0.06 mm, 99.9% purity) was used as counter electrode at 25 °C. All potentials are referred to the reversible hydrogen electrode (RHE) scale and were *iR*-corrected to account for Ohmic losses. All films were coated on a spherical Ti chip of 5 mm diameter and mounted on a rotating disc shaft serving as a working electrode. Due to the fact that all electrocatalysts were directly synthesized as porous films on polished Ti substrates, the addition of Nafion binder was not necessary. A rotation of 1600 rpm was set. 0.5 M H_2SO_4 was used as a supporting electrolyte (Fixanal, Fluka Analytical) and a SP-200 (Biologic) was used as a potentiostat. The electrolyte solution was purged with N_2 for at least 20 min prior to catalytic testing. The OER activity was assessed by cyclic voltammetry (CV) in a potential window ranging between 1.20 and 1.65 V versus RHE (V_{RHE}) at a scan rate of 6 mV s^{-1}. Chronopotentiometry was performed in an RDE setup in 0.5 M H_2SO_4 over 24 h at 25 °C. The potential (vs RHE) was recorded at a current density j of 1.0 mA cm^{-2}, considering the ultra-low Ir loadings in the catalyst films.

Base Voltammetry for ECSA Estimation: After 100 CVs in OER regime, a base voltammetry measurement was performed in a lower potential range between 0.40 to 1.40 V_{RHE} at 25 °C for an estimation of the ECSA with a scan rate of 50 mV s^{-1}, according to a previously published method.[20,30] In brief, the calculated average value of the integrated anodic and cathodic scan of the recorded *iR*-corrected CVs ($q_{(a+c)/2}$) can be used to estimate the amount of accessible iridium sites for each catalyst film. This method relies on Faradaic currents of different Ir^{x+} redox active sites correlating with their abundancy and accessibility to the electrolyte.[30,66]

Preparation of a Homogeneous Ink for RDE Measurements of a Commercial Reference (Elyst, Umicore): To investigate the OER performance of the industrially relevant and commercially available Ir/TiO_2 catalyst powder (74.7 wt.-% Ir in TiO_2, Elyst Ir 75 0480, Umicore), a dispersion was prepared by suspending the black powder (5.4 mg) in a mixture of MilliQ-H_2O (2.49 mL), ^{i}PrOH (2.49 mL, > 99.5%, Carl Roth) and Nafion perfluorinated resin (20 µL, 5 wt-% in lower aliphatic alcohols and H_2O, Sigma Aldrich, 15–20% H_2O). A homogeneous ink of dark black color was obtained after the application of ultrasound for 10 min using an ultrasonic tip (Bandelin, Sonopuls). 5 µL of the ink were subsequently drop-casted at room temperature onto an extensively polished Ti cylinder with a geometric surface area of 0.1963 cm^{-2} and dried at 65 °C in a preheated drying oven in air for 10 min. This step was repeated between one to five times to afford nominal Ir loadings of

≈20 to 100 µg cm^{-2}. The assessment of catalytic OER activity in an RDE setup revealed a linear dependence of nominal Ir loading and current density *j* at a potential of 1.60 V_{RHE}.

Supporting Information

Supporting Information is available from the Wiley Online Library or from the author.

Acknowledgements

M.F. and M.H.R. contributed equally to this work. The authors acknowledge preliminary studies by Michael Bernicke (TU Berlin) on the synthesis of the mesoporous support films and subsequent ALD modifications. Arne Thomas (TU Berlin) is thankfully acknowledged for granting access to a setup for XPS analysis. Christoph Erdmann (HU Berlin) is acknowledged for TEM measurements. Leyla Kotil (TU Berlin) is thankfully acknowledged for the assistance in the calibration of the SEM-EDX measurements for the estimation of the geometric Ir loadings. The authors gratefully acknowledge financial support by BMBF (Bundesministerium für Bildung und Forschung) ATO-KAT: Atomar dünn beschichtete poröse Elektroden als neuartige Katalysatoren für die Wasser-Elektrolyse (03EK3052A). R.S. acknowledges generous funding from the project ATMOC (20IND04, Traceable metrology of soft X-ray to IR optical constants and nanofilms for advanced manufacturing). R.K. gratefully acknowledges funding through the DFG SPP 2080 priority program (KR 3920/4-1).

Open access funding enabled and organized by Projekt DEAL.

Conflict of Interest

The authors declare no conflict of interest.

Data Availability Statement

The data that support the findings of this study are available from the corresponding author upon reasonable request.

Keywords

acidic oxygen evolution reaction, atomic layer deposition, electrocatalysis, iridium oxide, soft-templated mesoporous films

Received: October 18, 2021
Revised: December 15, 2021
Published online: January 27, 2022

[1] I. Dincer, *Int. J. Hydrogen Energy* **2012**, *37*, 1954.
[2] R. Bhandari, C. A. Trudewind, P. Zapp, *J. Cleaner Prod.* **2014**, *85*, 151.
[3] K. Mazloomi, C. Gomes, *Renewable Sustainable Energy Rev.* **2012**, *16*, 3024.
[4] G. Glenk, S. Reichelstein, *Nat. Energy* **2019**, *4*, 216.
[5] F. Barbir, *Sol. Energy* **2005**, *78*, 661.
[6] S. Cobo, J. Heidkamp, P.-A. Jacques, J. Fize, V. Fourmond, L. Guetaz, B. Jousselme, V. Ivanova, H. Dau, S. Palacin, M. Fontecave, V. Artero, *Nat. Mater.* **2012**, *11*, 802.
[7] M. Carmo, D. L. Fritz, J. Mergel, D. Stolten, *Int. J. Hydrogen Energy* **2013**, *38*, 4901.
[8] A. L. Strickler, R. A. Flores, L. A. King, J. K. Nørskov, M. Bajdich, T. F. Jaramillo, *ACS Appl. Mater. Interfaces* **2019**, *11*, 34059.
[9] L. C. Seitz, C. F. Dickens, K. Nishio, Y. Hikita, J. Montoya, A. Doyle, C. Kirk, A. Vojvodic, H. Y. Hwang, J. K. Norskov, T. F. Jaramillo, *Science* **2016**, *353*, 1011.
[10] E. Ortel, T. Reier, P. Strasser, R. Kraehnert, *Chem. Mater.* **2011**, *23*, 3201.
[11] N. Mamaca, E. Mayousse, S. Arrii-Clacens, T. W. Napporn, K. Servat, N. Guillet, K. B. Kokoh, *Appl. Catal., B* **2012**, *111-112*, 376.
[12] M. A. Hubert, A. M. Patel, A. Gallo, Y. Liu, E. Valle, M. Ben-Naim, J. Sanchez, D. Sokaras, R. Sinclair, J. K. Nørskov, L. A. King, M. Bajdich, T. F. Jaramillo, *ACS Catal.* **2020**, *10*, 12182.
[13] Z. Shi, X. Wang, J. Ge, C. Liu, W. Xing, *Nanoscale* **2020**, *12*, 13249.
[14] R. A. Flores, C. Paolucci, K. T. Winther, A. Jain, J. A. G. Torres, M. Aykol, J. Montoya, J. K. Nørskov, M. Bajdich, T. Bligaard, *Chem. Mater.* **2020**, *32*, 5854.
[15] V. V. Panić, A. B. Dekanski, M. Mitrić, S. K. Milonjić, V. B. Mišković-Stanković, B. Ž. Nikolić, *Phys. Chem. Chem. Phys.* **2010**, *12*, 7521.
[16] A. Marshall, S. Sunde, M. Tsypkin, R. Tunold, *Int. J. Hydrogen Energy* **2007**, *32*, 2320.
[17] A. Marshall, B. Børresen, G. Hagen, M. Tsypkin, R. Tunold, *Electrochim. Acta* **2006**, *51*, 3161.
[18] A. Hartig-Weiss, M. Miller, H. Beyer, A. Schmitt, A. Siebel, A. T. S. Freiberg, H. A. Gasteiger, H. A. El-Sayed, *ACS Appl. Nano Mater.* **2020**, *3*, 2185.
[19] M. Bernicke, E. Ortel, T. Reier, A. Bergmann, J. Ferreira de Araujo, P. Strasser, R. Kraehnert, *ChemSusChem* **2015**, *8*, 1908.
[20] D. Bernsmeier, M. Bernicke, R. Schmack, R. Sachse, B. Paul, A. Bergmann, P. Strasser, E. Ortel, R. Kraehnert, *ChemSusChem* **2018**, *11*, 2367.
[21] C. Comninellis, G. P. Vercesi, *J. Appl. Electrochem.* **1991**, *21*, 335.
[22] S. Geiger, O. Kasian, A. M. Mingers, K. J. J. Mayrhofer, S. Cherevko, *Sci. Rep.* **2017**, *7*, 4595.
[23] C. Daiane Ferreira da Silva, F. Claudel, V. Martin, R. Chattot, S. Abbou, K. Kumar, I. Jiménez-Morales, S. Cavaliere, D. Jones, J. Rozière, L. Solà-Hernandez, C. Beauger, M. Faustini, J. Peron, B. Gilles, T. Encinas, L. Piccolo, F. H. Barros de Lima, L. Dubau, F. Maillard, *ACS Catal.* **2021**, *11*, 4107.
[24] M. Shao, Q. Chang, J.-P. Dodelet, R. Chenitz, *Chem. Rev.* **2016**, *116*, 3594.
[25] F. Lyu, Q. Wang, S. M. Choi, Y. Yin, *Small* **2019**, *15*, 1804201.
[26] C. J. Brinker, Y. Lu, A. Sellinger, H. Fan, *Adv. Mater.* **1999**, *11*, 579.
[27] T. Brezesinski, M. Groenewolt, A. Gibaud, N. Pinna, M. Antonietti, B. Smarsly, *Adv. Mater.* **2006**, *18*, 2260.
[28] C. Sanchez, C. Boissière, D. Grosso, C. Laberty, L. Nicole, *Chem. Mater.* **2008**, *20*, 682.
[29] E. Ortel, A. Fischer, L. Chuenchom, J. Polte, F. Emmerling, B. Smarsly, R. Kraehnert, *Small* **2012**, *8*, 298.
[30] M. Bernicke, D. Bernsmeier, B. Paul, R. Schmack, A. Bergmann, P. Strasser, E. Ortel, R. Kraehnert, *J. Catal.* **2019**, *376*, 209.
[31] M. Frisch, J. Laun, J. Marquardt, A. Arinchtein, K. Bauerfeind, D. Bernsmeier, M. Bernicke, T. Bredow, R. Kraehnert, *Phys. Chem. Chem. Phys.* **2021**, *23*, 3219.
[32] E. Ortel, J. Polte, D. Bernsmeier, B. Eckhardt, B. Paul, A. Bergmann, P. Strasser, F. Emmerling, R. Kraehnert, *Appl. Catal., A* **2015**, *493*, 25.
[33] S. M. George, *Chem. Rev.* **2010**, *110*, 111.
[34] M. Ritala, M. Leskelä, in *Handbook of Thin Film Materials*, Vol. 1, Academic Press, San Diego **2002**, pp. 103–159.
[35] N. Pinna, M. Knez, *Atomic Layer Deposition of Nanostructured Materials*, Wiley-VCH, Weinheim, Germany **2011**.
[36] C. Marichy, M. Bechelany, N. Pinna, *Adv. Mater.* **2012**, *24*, 1017.
[37] K. L. Pickrahn, S. W. Park, Y. Gorlin, H.-B.-R. Lee, T. F. Jaramillo, S. F. Bent, *Adv. Energy Mater.* **2012**, *2*, 1269.
[38] M. H. Raza, K. Movlaee, S. G. Leonardi, N. Barsan, G. Neri, N. Pinna, *Adv. Funct. Mater.* **2020**, *30*, 1906874.

[39] Y. Fan, Y. Wu, G. Clavel, M. H. Raza, P. Amsalem, N. Koch, N. Pinna, *ACS Appl. Energy Mater.* **2018**, *1*, 4554.
[40] G. N. Parsons, S. M. George, M. Knez, *MRS Bull.* **2011**, *36*, 865.
[41] J. Hämäläinen, T. Hatanpää, E. Puukilainen, T. Sajavaara, M. Ritala, M. Leskelä, *J. Mater. Chem.* **2011**, *21*, 16488.
[42] J. Hämäläinen, M. Ritala, M. Leskelä, *Chem. Mater.* **2014**, *26*, 786.
[43] F. Li, L. Li, X. Liao, Y. Wang, *J. Membr. Sci.* **2011**, *385-386*, 1.
[44] S. Schlicht, S. Haschke, V. Mikhailovskii, A. Manshina, J. Bachmann, *ChemElectroChem* **2018**, *5*, 1259.
[45] S. Schlicht, P. Büttner, J. Bachmann, *ACS Appl. Energy Mater.* **2019**, *2*, 2344.
[46] J. Hämäläinen, M. Kemell, F. Munnik, U. Kreissig, M. Ritala, M. Leskelä, *Chem. Mater.* **2008**, *20*, 2903.
[47] V. Pfeifer, T. E. Jones, J. J. Velasco Vélez, C. Massué, R. Arrigo, D. Teschner, F. Girgsdies, M. Scherzer, M. T. Greiner, J. Allan, M. Hashagen, G. Weinberg, S. Piccinin, M. Hävecker, A. Knop-Gericke, R. Schlögl, *Surf. Interface Anal.* **2016**, *48*, 261.
[48] H. Y. Hall, P. M. A. Sherwood, *J. Chem. Soc., Faraday Trans. 1* **1984**, *80*, 135.
[49] H. Cesiulis, N. Tsyntsaru, A. Ramanavicius, G. Ragoisha, in *Nanostructures and Thin Films for Multifunctional Applications: Technology, Properties and Devices* (Eds: I. Tiginyanu, P. Topala, V. Ursaki), Springer, Berlin **2016**, pp. 3–42.
[50] S. Fierro, L. Ouattara, E. H. Calderon, C. Comninellis, *Electrochem. Commun.* **2008**, *10*, 955.
[51] R. Sachse, M. Pflüger, J.-J. Velasco-Vélez, M. Sahre, J. Radnik, M. Bernicke, D. Bernsmeier, V.-D. Hodoroaba, M. Krumrey, P. Strasser, R. Kraehnert, A. Hertwig, *ACS Catal.* **2020**, *10*, 14210.
[52] S. Schlicht, M. K. S. Barr, M. Wu, P. Hoppe, E. Spiecker, W. Peukert, J. Bachmann, *ChemElectroChem* **2018**, *5*, 3932.
[53] D. Bernsmeier, M. Bernicke, E. Ortel, A. Bergmann, A. Lippitz, J. Nissen, R. Schmack, P. Strasser, J. Polte, R. Kraehnert, *ChemElectroChem* **2017**, *4*, 221.
[54] A. Rossi, J. F. C. Boodts, *J. Appl. Electrochem.* **2002**, *32*, 735.
[55] A. G. Hufnagel, S. Häringer, M. Beetz, B. Böller, D. Fattakhova-Rohlfing, T. Bein, *Nanoscale* **2019**, *11*, 14285.
[56] C. Van Pham, M. Bühler, J. Knöppel, M. Bierling, D. Seeberger, D. Escalera-López, K. J. J. Mayrhofer, S. Cherevko, S. Thiele, *Appl. Catal., B* **2020**, *269*, 118762.
[57] W. Hu, S. Chen, Q. Xia, *Int. J. Hydrogen Energy* **2014**, *39*, 6967.
[58] E. Oakton, D. Lebedev, M. Povia, D. F. Abbott, E. Fabbri, A. Fedorov, M. Nachtegaal, C. Copéret, T. J. Schmidt, *ACS Catal.* **2017**, *7*, 2346.
[59] D. Böhm, M. Beetz, M. Schuster, K. Peters, A. G. Hufnagel, M. Döblinger, B. Böller, T. Bein, D. Fattakhova-Rohlfing, *Adv. Funct. Mater.* **2020**, *30*, 1906670.
[60] H. N. Nong, H.-S. Oh, T. Reier, E. Willinger, M.-G. Willinger, V. Petkov, D. Teschner, P. Strasser, *Angew. Chem., Int. Ed.* **2015**, *54*, 2975.
[61] L. Yang, G. Yu, X. Ai, W. Yan, H. Duan, W. Chen, X. Li, T. Wang, C. Zhang, X. Huang, J.-S. Chen, X. Zou, *Nat. Commun.* **2018**, *9*, 5236.
[62] P. E. Pearce, C. Yang, A. Iadecola, J. Rodriguez-Carvajal, G. Rousse, R. Dedryvère, A. M. Abakumov, D. Giaume, M. Deschamps, J.-M. Tarascon, A. Grimaud, *Chem. Mater.* **2019**, *31*, 5845.
[63] P. Lettenmeier, J. Majchel, L. Wang, V. A. Saveleva, S. Zafeiratos, E. R. Savinova, J.-J. Gallet, F. Bournel, A. S. Gago, K. A. Friedrich, *Chem. Sci.* **2018**, *9*, 3570.
[64] E. Ortel, A. Hertwig, D. Berger, P. Esposito, A. M. Rossi, R. Kraehnert, V.-D. Hodoroaba, *Anal. Chem.* **2016**, *88*, 7083.
[65] R. Sachsé, A. Hertwig, R. Kraehnert, V.-D. Hodoroaba, *Microsc. Microanal.* **2018**, *24*, 762.
[66] S. Ardizzone, A. Carugati, S. Trasatti, *J. Electroanal. Chem. Interfacial Electrochem.* **1981**, *126*, 287.